CARBON 79 (2014) 85–92

Available at www.sciencedirect.com

ScienceDirect

journal homepage: www.elsevier.com/locate/carbon

Nano-scale mapping of lattice strain and orientation inside carbon core SiC fibres by synchrotron X-ray diffraction

Nikolaos Baimpas [a,*], Alexander J.G. Lunt [a], Igor P. Dolbnya [b], Jiri Dluhos [c], Alexander M. Korsunsky [a]

[a] Department of Engineering Science, University of Oxford, Parks Road, Oxford OX1 3PJ, UK
[b] Diamond Light Source, Harwell Science and Innovation Campus, Didcot, Oxfordshire OX11 0DE, UK
[c] TESCAN Brno, s.r.o., Libušina třída 1, 623 00 Brno, Czech Republic

ARTICLE INFO

Article history:
Received 9 April 2014
Accepted 15 July 2014
Available online 22 July 2014

ABSTRACT

The strongest fibres available today are carbon-based, made from carbon nanotubes (CNTs) or reduced graphene oxide flakes (RGOFs). Carbon fibres (CFs) were first developed half a century ago. Control of the thermal, chemical and mechanical processing allows obtaining desired combination of structure, strength and stiffness. In practical use, CFs are typically incorporated into larger scale systems that require multi-scale characterisation. In the present study we considered an aerospace composite consisting of titanium alloy matrix reinforced with unidirectional silicon carbide fibres with carbon monofilament core. By combining synchrotron-based imaging and nano-focused X-ray beam scattering with Focused Ion Beam stress evaluation, we construct detailed maps of structure and strain inside this material. Eigenstrain modelling was used to reconstruct the full residual strain state within the fibre cross-section. The joined-up experimental and theoretical approach allows extracting information about fibre structure down to the nanoscale, developing insight into its processing history, and revealing the existence of significant residual strains that have a strong effect on the performance of CFs in service.

1. Introduction

Much of the present understanding of the morphology and texture in carbon fibres derives from TEM investigations that reveal the lattice properties and arrangement at the nanoscale [1–3]. In practical use CFs are incorporated into larger scale systems, e.g. as cores of silicon carbide fibres for aerospace composite applications or woven into fabric reinforcement in high performance polymer matrix composites for motor sports, etc. The ability to characterise the hierarchical, multi-scale structure of carbon fibres that serve as the reinforcement basis in composite systems remains a challenge. Synchrotron X-ray beams offer an excellent combination of flux, brightness and energy for nanoscale imaging alignment and spatially resolved diffraction mapping [4]. However, the co-existence of crystalline and amorphous content in CFs makes nanoscale characterisation using a single technique insufficient [5].

Carbon fibres can be made via different routes that depend on the choice of precursor. PAN-based carbon fibres are made

* Corresponding author.
E-mail address: nikolaos.baimpas@gmail.com (N. Baimpas).
http://dx.doi.org/10.1016/j.carbon.2014.07.045
0008-6223/

by pyrolytic reduction of polyacrylonitrile (PAN) fibres. The resulting carbon fibres contain a mixture of amorphous and crystalline material, with the maximum crystalline volume fraction of 50% [6]. Alternatively, CFs can be produced by carbonization of mesophase pitch (MPP), a carbonaceous precursor with a highly oriented crystal structure [7]. Both PAN and MPP precursors are subjected to subsequent processing including spinning (melt–wet–dry), coagulation bath, drawing and curing in the as-spun state. Control over process parameters such as fibre elongation (draw-down rate) results in fibres with different morphologies (different void content and preferred orientation), with the degree of carbonization (crystalline content) reaching up to 80% (>2000 °C) [8,9].

The principal distinction between the nanostructure of PAN-based and pitch-based CFs is the degree of crystallinity and preferred orientation. PAN-based CFs with random crystal orientation and significant amorphous content display high strength and moderate modulus [3]. The highly aligned MPP-based fibres have the combination of high modulus and moderate strength. In the present study, focused X-ray beam mapping of the carbon monofilament core of SCS-6 silicon carbide fibres reveals a transition from the central untextured region of ~13.5 μm diameter (with a structure similar to a PAN-based CF) to a more highly aligned and crystalline outer region of ~35 μm diameter (with a structure similar to a MPP-based CF). Thus the carbon monofilament core combines the two morphologies.

The combination of strength and stiffness of SiC fibres makes them a competitive material choice for unidirectional reinforcement of metal matrix composites for high value aerospace and automotive applications. Over the last few decades, SiC fibre-reinforced titanium alloy matrix composites have undergone intensive development and found a number of advanced applications. The composite investigated in the present study consisted of a Ti-6Al-4V alloy matrix reinforced with 35% by volume SCS-6 SiC fibres that increase the stiffness in the longitudinal direction from ~115 GPa to ~210 GPa [10], offering considerable weight savings. Experimental studies of the mechanical behaviour of this composite have been reported previously, e.g. during fatigue experiments at elevated temperatures up to 350 °C [11]. SiC fibres make the most significant contribution to the mechanical properties of the composite.

2. Experimental setup – methods

2.1. *Experimental setup*

The combined synchrotron imaging and scattering experiment (Fig. 1) was conducted on the Test Beamline B16 at Diamond Light Source, Harwell Science and Innovation Campus, UK (MT-9318). The bending magnet delivers X-ray flux with smooth spectral distribution in the range between 8 keV and 25 keV. The beam can be passed through a double crystal monochromator, or above it at the fixed offset of 25 mm in the white beam mode. Focusing in both modes can be achieved using a Kirkpatrick–Baez (KB) mirror pair. The mirrors are operated at a nominal 3mrad incidence angle and consist of a pair of elliptical pre-shaped silicon substrates coated with 40 nm thick Pt layer. Prior to collecting scattering data in the line scanning or mapping modes, the relative position of the focused beam is determined with respect to the main beam in the focal plane XY that is located 55 mm downstream from the edge of the KB mirror chamber. A set of 200 μm diameter tungsten cross-wires is mounted on the XY translation stage. This arrangement allows precise determination of the beam position (x_{KB}, y_{KB}) with respect to the main beam, as well as its size (see Fig. S1 in the Supplementary Material). In front of the cross-wires, there is a 150-μm diameter guard pinhole, made in tungsten plate, that lets through the focused beam, whilst blocking the weak remains of main direct beam and single reflections of the mirrors. Both the cross-wires and the pinhole are placed on magnetic kinematic mounts that allow them to be repeatedly removed and repositioned to better than micron accuracy. The position of the cross-wires along the Z axis collinear with the main beam is marked to micron precision by a theodolite. It is used to place the specimen in the correct Z position (the focal plane).

The KB-mirror chamber is mounted on a motorised translation stage that allows its precise movement in both vertical and horizontal planes in and out of the main beam for focusing and radiographic imaging of the specimen, respectively. A host of different detectors are mounted simultaneously and used in accordance with the task. Imaging detectors used in the present experiment were the "X-ray eye" ($6.4 \times 6.4\ \mu m^2$ pixel size X-ray CCD miniFDI camera from Photonic Science Ltd). This detector is particularly useful for preliminary radiographic sample alignment due to its fast readout time. For higher resolution imaging, a PCO 4000 camera coupled to the Optique Peter microscope (an objective lens – 10× magnification, $0.9 \times 0.9\ \mu m^2$ effective pixel size) and a 35-μm thick YAG(Ce) scintillator were used. For X-ray diffraction data acquisition, the Photonic Science ImageStar 9000 high-resolution X-ray CCD detector ($31 \times 31\ \mu m^2$ pixel size) was used (raw experimental results are given on Fig. S2). A small photodiode could also be mounted on the beam-stop of the detector as required.

The sample is first positioned approximately using lasers that indicated coarsely the position of the collimated beam. With the main beam passing outside the KB mirror chamber, the two sets of collimation slits were placed wide open to expose the full field of view of the "X-ray eye". Sample stage tilting around the X-axis and rotation around the Y-axis were used to achieve best possible fibre alignment parallel to the beam. By progressive reduction of the beamsize (from 3.2×3.2 mm down to 10×10 μm), the core carbon monofilament is brought into alignment with the centre of the main beam. The procedure is continued to improve the alignment down to 1 μm and better by using the PCO camera detector for imaging.

The unstrained values of the c lattice parameter values used for strain evaluation were $c_0^i = 6.9980$ Å for the inner carbon region, and $c_0^o = 6.8353$ Å for the outer carbon region as determined by the diffraction data. The reference value of the a_0 lattice parameter in the fcc SiC using X-ray diffraction data was taken to be $a_0 = 4.3982$ Å. Interplanar spacing values corresponding to the diffraction peaks 002 and 111 were

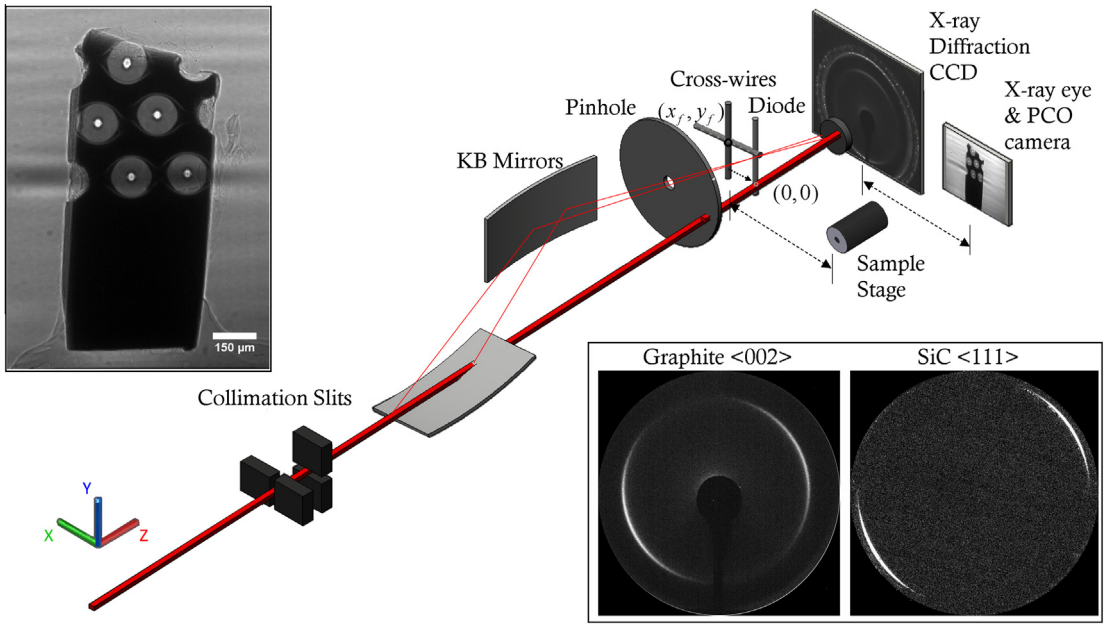

Fig. 1 – Setup for simultaneous X-ray imaging and diffraction using synchrotron beam: beam collimation, focusing and alignment. Examples of diffraction patterns are shown as insets. (A colour version of this figure can be viewed online.)

used for strain evaluation in the carbon monofilament and SiC coating, respectively.

The crystallite size was determined using the Scherrer formula [12],

$$L_c = \frac{(0.91)\lambda}{\beta \cos\theta} \quad (1)$$

where λ is the wavelength (nm), β is the Full Width at Half Maximum (FWHM), and θ is half of the scattering angle (radians).

2.2. *Focused Ion Beam (FIB)–Digital Image Correlation (DIC) for residual strain evaluation*

Following careful sample surface preparation and polishing down to 0.1 μm colloidal silica the micro-ring-core Focused Ion Beam (FIB) and Digital Image Correlation (DIC) technique was performed using a Tescan LYRA3 SEM-FIB. FIB milling of six 4 × 4 μm islands (three in the SiC and three in the neighbouring carbon region) was then performed using a 'ladder' like mask (Fig. 2a and b). An island size of 4 μm was selected as a balance between strain spatial resolution and providing sufficient surface area to produce a reliable estimate of strain relief. A trench width of 1 μm and a milling current of 1 nA was chosen to reduce the impact of material re-deposition. It can be readily observed by the high-resolution micrographs of the FIBed region before and after milling illustrated in Fig. 2 shows minimum damage on the surface of the island. In order to improve surface contrast and topology a beam voltage of 10 kV was used to image the sample and over 340 high resolution SEM micrographs were captured obtained at 52° tilt of the stage. It was found that the Z-contrast between the carbon in specimen surface and embedded colloidal silica nano-particles was sufficient to enable effective DIC of these micrographs. Several thousand markers were seeded onto these images and, following manual and automated outlier removal, a tracking script was used to determine the surface strain relief in each of the islands in the hoop (i.e. circumferential) and radial direction (as a function of image number). Least-squares fitting of known strain relief profiles [13] was then used to determine the average full strain relief in each island and to provide an estimate of confidence intervals on each measurement.

In order to provide calibration for the strain-free lattice parameters in the CF the micro-ring core FIB and DIC technique was implemented at the interface between the central SiC and the neighbouring carbon region. This method relies on an incremental FIB milling process to fully stress relieve micro to nano-scale islands of material on the specimen surface [14]. During this procedure, high resolution micrographs of this region are collected which are later processed using DIC software to provide a direct measurement of the average complete radial and hoop strain relief experienced by the islands. Novel arrangement of these stress relieved regions in the form of a 'ladder' has enabled, for the first time, the production of maps of residual strain that at the spatial resolution of a few microns (Fig. 2c and d). The amount of strain relief after milling provides the measure of the residual elastic strain present within the material prior to FIB milling. The knowledge of this strain from FIB–DIC, together with the diffraction data obtained at the same location, allows the strain-free lattice parameter values (a_0, c_0^1 and c_0^0)) to be calculated.

2.3. *Inverse eigenstrain modelling approach*

Consider an axisymmetric elastic fibre occupying the region $-x_r < x < x_r$, $-\infty < y < \infty$ and containing a distribution of radially varying eigenstrain $\varepsilon^*_{rr}(r) = \varepsilon^*_{\theta\theta}(r)$. The inverse eigenstrain modelling framework presented in [15] was used, with modifications explained here. An axi-symmetric plane strain Finite

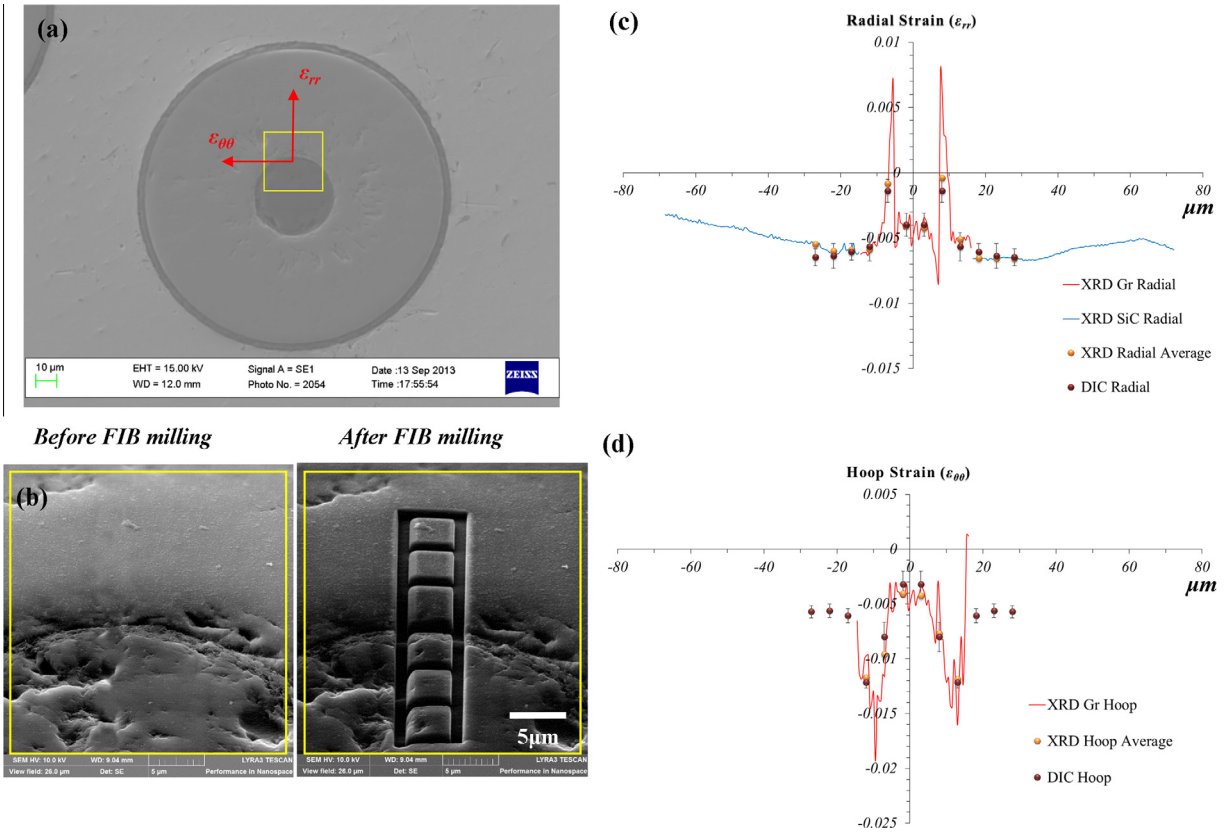

Fig. 2 – Focused Ion Beam milling–Digital Image Correlation and XRD measurement and FE modelling results: SEM image (a) indicating the locating of FIB analysis where "ladder" pattern (b) was milled at the interface of SiC and carbon in order to determine the radial and hoop residual strain components for calibration and validation of the X-ray diffraction results (c and d). (A colour version of this figure can be viewed online.)

Element Model was created. The Ti-6Al-4V alloy matrix that contained the fibres was not included in the model, due to its very limited influence on the in-plane residual elastic strains in the SCS fibres. The FE model for the SCS fibre consisted of three different regions with distinct properties. The material occupying the inner and outer carbon regions were assigned Young's modulus of 41 GPa and Poisson's ratio ν of 0.4. The outer SiC part was assigned Young's modulus of 380 GPa and Poisson's ratio υ of 0.2. Element type CAX8R was used for the simulation. The basis functions for inversion were obtained from the solution of the direct eigenstrain problem for each individual "tent function" [16] corresponding to the peak eigenstrain values of $\varepsilon^*_{rr} = \varepsilon^*_{\theta\theta} = 10^{-3}$. The tent functions were installed in the FE model as axisymmetric bands of local pseudo-thermal strain at radial position increments of 1 µm between 0 and 70 µm.

The solution for the inverse eigenstrain problem was sought by minimising the penalty function (Eqs. (2) and (3)) that represents the mismatch between the model prediction and experimental measurement (Fig. S3).

$$J = \sum_{j=1}^{m} w_j (y_j - e_j)^2 \tag{2}$$

$$J = \sum_{j=1}^{m} w_j \left(\sum_{i=1}^{N} c_i e_{ij} - y_j \right)^2 \tag{3}$$

The unknown coefficients c_i of each tent function in the linear combination were sought by minimising the penalty function (Eq. (4)) as follows:

$$\nabla_c J = 0 \Rightarrow \frac{\partial J}{\partial c_i} = 0, i = 1, 2, \ldots, N \tag{4}$$

It is worth noting that the quadratic form of the penalty function ensures that the system of Eq. (4) above always has a unique solution in terms of the vector of unknown coefficients c_i.

3. Results and discussion

The body of work reported above represents the synthesis of several high resolution experimental techniques using particle beams (scanning ion and electron microscopy and scanning synchrotron X-ray diffraction) with advanced numerical modelling. Only such combined approach enables deep integration of the data across multiple scales, and the construction of the overall consistent picture of the structural and residual stress state of advanced carbon fibre-based material systems. An important feature of the results reported here is that no data of comparable resolution and detail could be found anywhere in the literature. In this situation the authors have sought different ways to check the results for internal consistency and robustness.

The synthetic Fig. 3 illustrates the nanostructure of the carbon monofilament core in terms of the spatial distribution of the crystalline particle size and shape, lattice orientation (Fig. S4 and Figs. 4b and 5b) and the crystalline volume fraction [17]. The insight embedded in this image has profound implications for structural integrity and performance in service. These implications are discussed in some detail below.

Carbon fibres can be used in a wide variety of applications ranging from lithium ion batteries to polymer matrix composites. The complex nanostructure of the fibre (Fig. 3) suggests that deformation analysis must take into account the multi-scale load transfer mechanisms between the crystallites and the surrounding amorphous "matrix", as well as the interaction between the unoriented central region and the surrounding highly textured material [18]. Furthermore, significant residual stresses are likely to be present within the system, having implications for its deformation response and the ultimate strength in tension and compression. Measuring these residual stresses is not a trivial task, since they vary at sub-micron length scales. X-ray diffraction can be used to evaluate the lattice interplanar spacing. However, the conversion of the results into elastic strains and residual stresses remains a challenge due to the impossibility of using a strain-free powder reference, the lattice parameter changes due to chemistry variation, and the load-bearing contribution of the amorphous content. To overcome these challenges, the present study employs a combination of nano-focused synchrotron X-ray beams with Focused Ion Beam (FIB) milling and Digital Image Correlation (DIC) analysis for direct residual strain evaluation [13]. The FIB–DIC technique does not require strain-free reference samples [19] and copes equally well with crystalline and amorphous components.

Published reports on carbon fibres describe experimental setups whereby the probing X-ray beam is directed at the fibre perpendicularly to its axis [4,20]. Due to the lack of gauge volume definition along the beam direction this produces diffraction patterns resulting from integrating the contributions from different radial positions within the fibre. High resolution mapping of the fibre structure and strain is impossible in this setup. Furthermore, without the knowledge of d_0 variation the interpretation of the results is of limited value. To overcome these difficulties we performed high resolution mapping of fibre cross section, as illustrated in Figs. 4 and 5. In order to achieve high resolution, careful alignment of the fibre axis with the incident X-ray beam was essential. Initial characterisation of the sample structure was carried out using X-ray tomography. It reveals the multi-layer fibre structure (Fig. 4a) consisting of the C monofilament core, SiC fibre bulk, and outer C coating at the interface between SiC and titanium alloy matrix. Next the sample was placed on a high resolution, six degree-of-freedom tomography stage with the beam travelled along the carbon monofilament core. Using high resolution imaging detector and monitoring the integrated transmitted intensity, alignment to better than 100 nm along the 300 μm fibre extent was achieved between the beam direction and the fibre axis (see inset in Fig. 1).

The SiC fibres with carbon monofilament cores embedded in the titanium alloy matrix are shown at different magnification in Fig. 4a that combines the results of SEM imaging with local tomographic rendering. It is important to note that the inner carbon region has similar electron density to the outer carbon layer in the monofilament, leading to very low contrast in electron and X-ray imaging modes alike (Fig. S5). However, X-ray diffraction provides clear discrimination that serves as the basis for the schematic illustration.

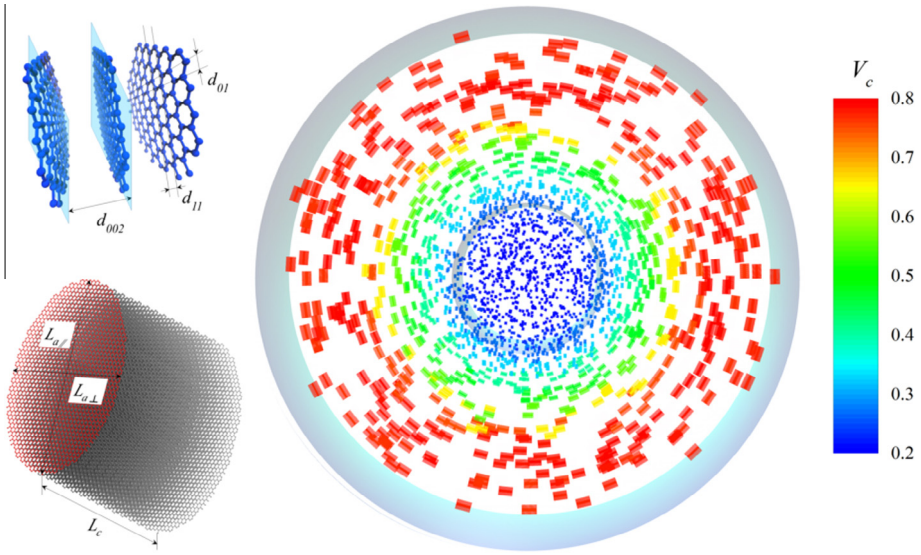

Fig. 3 – Nanostructure of the 35 μm diameter carbon fibre: the crystallite content V_c is shown by the colour. The lattice spacing parameters d_{01}, d_{11}, d_{002} are indicated in the upper inset showing the structure of the smallest sized crystallite. The shapes in the main figure illustrate the aspect ratio of the crystallites as viewed along the fibre axis. The crystallites have the dimensions L_c, $L_{a\parallel}$, and $L_{a\perp}$, as shown in the lower inset. For illustration purposes, the size of the crystallites in the main figure was exaggerated 1000×, and the number density shown is proportional to the local crystalline volume fraction divided by the average volume of individual crystallites. (A colour version of this figure can be viewed online.)

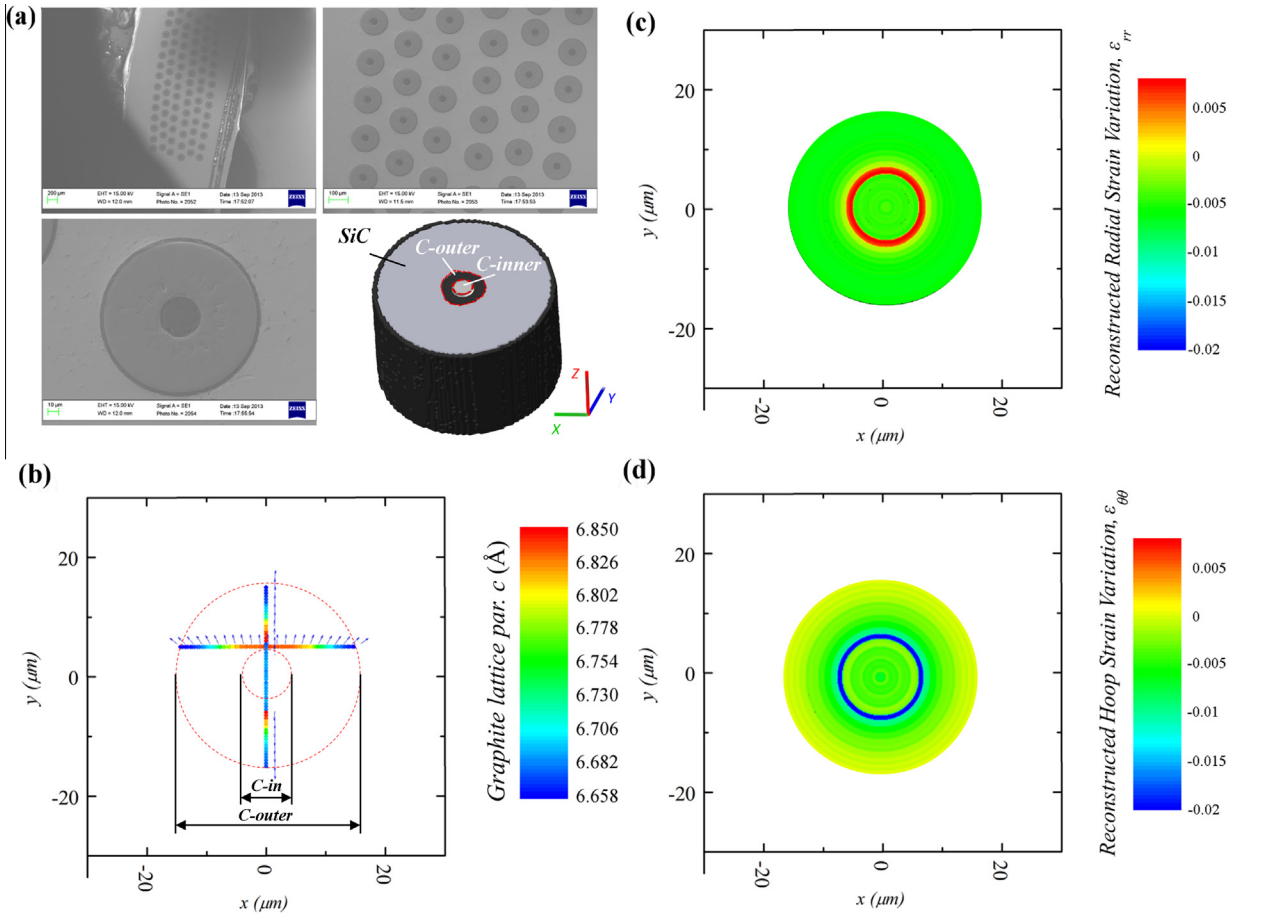

Fig. 4 – Residual elastic strain analysis in the carbon monofilament: SEM imaging and tomography reconstruction of the carbon core indicated in (a). The diffraction data collection points are indicated in (b). Figures (c) and (d) show eigenstrain reconstructions of the hoop $\theta\theta$ and radial *rr* elastic strains in the carbon fibre, respectively. (A colour version of this figure can be viewed online.)

Following sample alignment the position on the sample of the X-ray beam focused by Kirkpatrick–Baez (KB) mirrors was determined to better than 500 nm. The diffraction patterns were recorded and indexed for different regions on the sample (the inner and outer carbon regions, and SiC), and the integrated diffracted intensity scan was correlated with the sample radiographic image in order to determine the positions of the scanning lines. A grid was defined consisting of three vertical and three horizontal lines that were scanned at the step of 400 nm vertically and 500 nm horizontally. Different exposure times were carefully selected for different regions of the specimen to ensure optimal statistics (10 s for the SiC, 40 s for the carbon monofilament core). To obtain detailed mapping of the outer carbon layer and to avoid unnecessary data overlap, the middle horizontal line scan was offset by 5 μm with respect to the fibre centre. This offset was chosen in view of the typical diameter of PAN-based carbon fibres, in order to capture the detail of the preferred orientation and residual strain variation in the outer carbon region. The details of interpretation procedures applied to the diffraction patterns are supplied as Appendix A. Supplementary data. Sampling positions, lattice parameter variation, crystalline volume fraction and the preferred orientation of the 002 plane normal are shown on Fig. 4b.

Residual stress evaluation requires converting the lattice parameter into elastic strain using the unstrained lattice parameter value, d_0. The inner and outer regions in the carbon fibre are distinct and show a significant peak shift that exceeds the maximum strain-induced change that can be expected. This indicates that different strain-free lattice parameters (d_0^i and d_0^o) must be used for accurate strain calibration. Calibration was achieved by FIB nano-milling at the specimen surface to create a series ("ladder") of strain-relieved islands arranged along the fibre radius [19]. Digital Image Correlation (DIC) processing of the images collected before, during and after nano-milling revealed the residual elastic strain profiles at 4 μm spatial resolution used to calibrate the X-ray diffraction measurements. The complete dataset for the residual elastic strain profiles along the six horizontal and vertical scan lines was used as input into the inverse eigenstrain analysis procedure [15] described in the Methods section.

The reconstruction of the complete axisymmetric elastic strain state of the carbon fibre (radial ε_{rr} and hoop $\varepsilon_{\theta\theta}$ strain components) is shown in Fig. 4c and d. The glassy core of the carbon monofilament finds itself under mildly compressive hydrostatic strain of $\sim 4 \times 10^{-3}$. At the transition from the glassy inner region to the more crystalline outer carbon

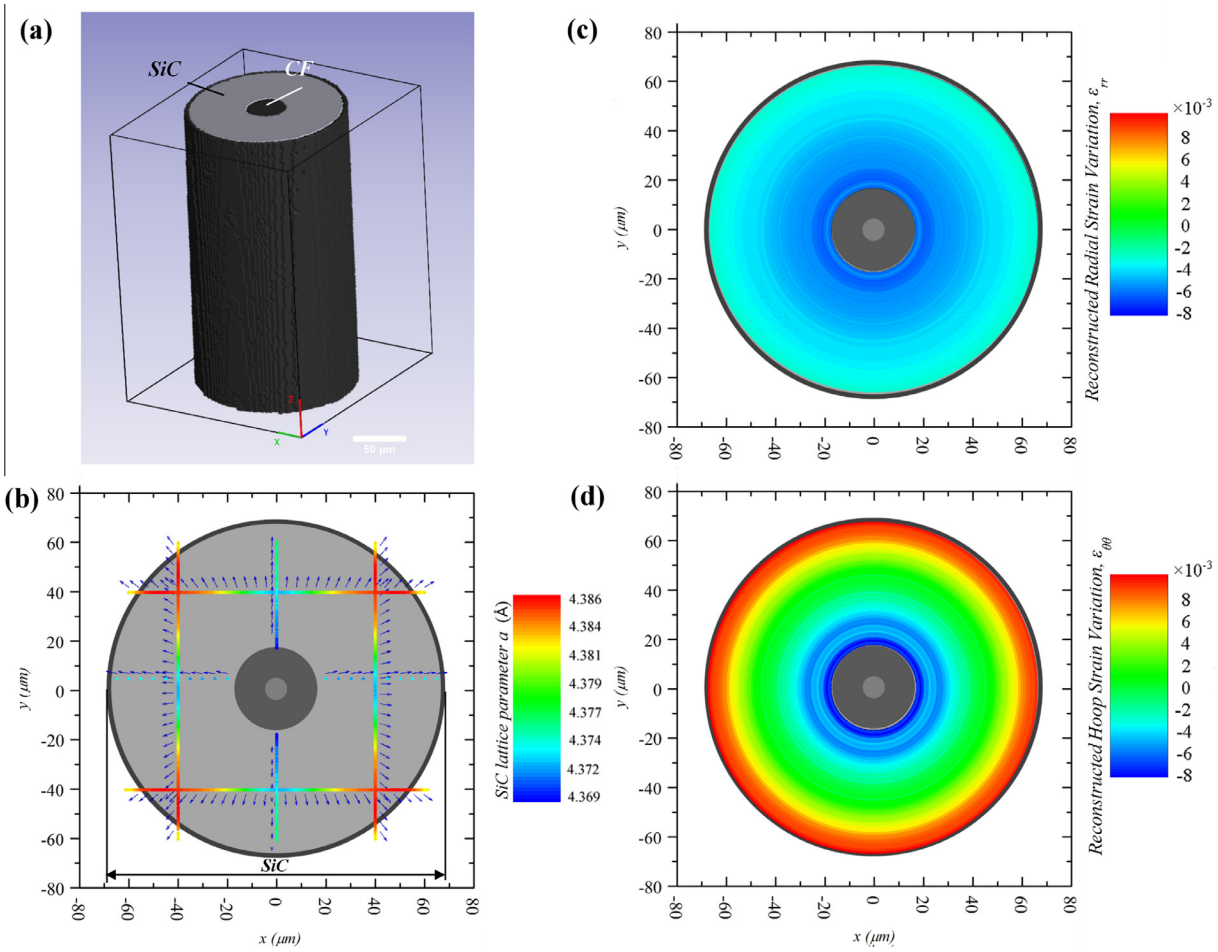

Fig. 5 – Residual elastic strain analysis in the SiC fibre: tomographic reconstruction (~0.9 μm resolution) showing carbon core (dark) and SiC outer layer (light grey). In (b) the inner light grey region represents the original PAN filament, with the outer layer representing carbon grown from pitch. Based on the diffraction data collected at locations shown in (b), figures (c) and (d) show maps of ($\theta\theta$) and radial (rr) elastic strain components, respectively. (A colour version of this figure can be viewed online.)

layer, a sharp strain gradient is found close to the interface, with the compressive hoop strain in excess of 1% (equivalent to 0.75 GPa compressive stress). The dual structure of the carbon monofilament results in a reduction in both the ultimate tensile strength (UTS = 0.86 GPa) and Young's Modulus (E = 41.5 GPa [21]). This is due to the fact that the monofilament manufacturing route was optimised in terms of the surface properties suitable for subsequent addition of the outer SiC layer. The observed mild linear variation of the hoop and radial residual elastic strains is likely to be associated with the radial growth of the fibre during the carbonization process. Overall, the observations suggest that the source of significant compressive stress in the carbon monofilament is associated with the presence of the outer SiC layer.

The 135 μm diameter SCS-6 SiC fibre was built around the carbon monofilament by CVD deposition. The growth of SiC grains proceeds in the radial direction, resulting in the highly aligned morphology and texture (preferred orientation), with the 111 plane normals pointing outwards, as illustrated in the quiver plot in Fig. 5b. Fig. 5a shows a tomographic rendering of the entire SCS-6 fibre (with the SiC layer shown in grey and carbon monofilament in black). It is worth noting the presence of a ~3 μm-thick outer layer that consists of the mixture of SiC and C that is deposited in order to improve the bonding to the alloy matrix during fibre incorporation into a composite structure [11,22].

Fig. 5b reports the results of lattice parameter mapping in the SiC layer. The built-in thermal misfit strains (eigenstrains) arise in the course of the CVD process, with additional thermal mismatch stresses developing during cooling from the deposition temperature due to the difference in the linear coefficients of thermal expansion ($\alpha_C \sim 2 \times 10^{-6}\,K^{-1}$, $\alpha_{SiC} \sim 4 \times 10^{-6}\,K^{-1}$) [23]. The distribution of eigenstrains that acts as the source of residual stress was determined by the inverse formulation [14]. The complete reconstruction of the residual strain distributions are shown in Fig. 5c and d. It is apparent that the outer layers of SiC sustain significant tensile hoop strains that place the middle section of the fibre into compression (cf. the results for the carbon monofilament reported above). Residual elastic hoop strain (also calibrated in the SiC by FIB–DIC) increases approximately linearly towards the

outer layers of the fibre, reaching the value of $\sim 5 \times 10^{-3}$ at the outer circumference of the SiC layer.

4. Conclusions

In conclusion, the suite of experimental and modelling analysis tools presented in this report allows detailed characterisation of both the structure and elastic strain across the scales within a complex hierarchical material. The intricate interplay between material growth and structure evolution, on the one hand, and the residual elastic strains locked within the system, on the other, determines both the stiffness and strength properties that ensue. Furthermore, a finite element model together with inverse eigenstrain analysis allows insight to be developed into the processing history and the origins of the high level residual strains within the fibre. The ability for detailed characterisation of these internal elastic strains is the first and crucial step towards developing exquisite control over the final properties by means of elastic strain engineering [24], and to designing better materials for superior performance.

Acknowledgements

The authors would like to thank Konstantinos Ritos, PhD student, University of Strathclyde, Glasgow, UK for his assistance in visualizing the carbon crystallites (insets in Fig. 2) using VMD software.

Appendix A. Supplementary data

Supplementary data associated with this article can be found, in the online version, at http://dx.doi.org/10.1016/j.carbon.2014.07.045.

REFERENCES

[1] Deurbergue A, Oberlin A. TEM study of some recent high modulus pan-based carbon fibers. Carbon 1992;30(7):981–7.
[2] Fortin F, Yoon SH, Korai Y, Mochida I. Structure of round-shaped methylnaphthalene-derived mesophase pitch-based carbon fibres prepared by spinning through a Y-shaped die hole. J Mater Sci 1995;30(18):4567–83.
[3] Fitzer E. Pan-based carbon fibers – present state and trend of the technology from the viewpoint of possibilities and limits to influence and to control the fiber properties by the process parameters. Carbon 1989;27(5):621–45.
[4] Loidl D, Peterlik H, Müller M, Riekel C, Paris O. Elastic moduli of nanocrystallites in carbon fibers measured by in-situ X-ray microbeam diffraction. Carbon 2003;41(3):563–70.
[5] Tanaka F, Okabe T, Okuda H, Ise M, Kinloch IA, Mori T, et al. The effect of nanostructure upon the deformation micromechanics of carbon fibres. Carbon 2013;52:372–8.
[6] Chung DDL. Carbon Fiber Composites. Butterworth-Heinemann; 1994.
[7] Matsumoto T. Mesophase pitch and its carbon fibers. Pure Appl Chem 1985;57(11):1553–62.
[8] Edie DD. Fibers and Composites. In: Delhaes Pierre, editor. CRC Press; 2003. http://dx.doi.org/10.1201/9780203166789.ch2. eBook ISBN: 978-0-203-16678-9.
[9] Edie DD. The effect of processing on the structure and properties of carbon fibers. Carbon 1998;36(4):345–62.
[10] Kaya F, Bowen P. Effect of increased interfacial strength on the fatigue crack growth resistance and crack opening displacement of β Ti21S/SCS 6 composites. Mater Sci Eng A 2008;476(1–2):301–7.
[11] Hutson A, John R, Jira J. Effect of temperature on fiber/matrix interface sliding stress in SCS-6/Timetal®21S. Scripta Mater 1999;40(5):529–35.
[12] Klug HP, Alexander LE. X-Ray Diffraction Procedures: For Polycrystalline and Amorphous Materials. 2nd ed. Wiley; 1974.
[13] Korsunsky AM, Sebastiani M, Bemporad E. Focused ion beam ring drilling for residual stress evaluation. Mater Lett 2009;63(22):1961–3.
[14] Song X, Yeap KB, Zhu J, Belnoue J, Sebastiani M, Bemporad E, et al. Residual stress measurement in thin films at sub-micron scale using Focused Ion Beam milling and imaging. Thin Solid Films 2012;520(6):2073–6.
[15] Korsunsky AM, Regino GM, Nowell D. Variational eigenstrain analysis of residual stresses in a welded plate. Int J Sol Struct 2007;44(13):4574–91.
[16] Song Xu, Chardonnet Solène, Savini Giancarlo, Zhang Shu Yan, Vorster Willem JJ, Korsunsky AM. Experimental/modelling study of residual stress in Al/SiCp bent bars by synchrotron XRD and slitting eigenstrain methods. Mater Sci Forum 2008;277:571–2.
[17] Takaku A, Shioya M. X-ray measurements and the structure of polyacrylonitrile- and pitch-based carbon fibres. J Mater Sci 1990;25(11):4873–9.
[18] Paris O, Loidl D, Peterlik H. Texture of PAN- and pitch-based carbon fibers. Carbon 2002;40(4):551–5.
[19] Baimpas N, Le Bourhis E, Eve S, Thiaudière D, Hardie C, Korsunsky AM. Stress evaluation in thin films: micro-focus synchrotron X-ray diffraction combined with focused ion beam patterning for do evaluation. Thin Solid Films 2013;549:245–50.
[20] Davies RJ, Riekel C, Koziol KK, Vilatela JJ, Windle AH. Structural studies on carbon nanotube fibres by synchrotron radiation microdiffraction and microfluorescence. J Appl Crystallogr 2009;42(6):1122–8.
[21] SPECIALTY MATERIALS I. [cited; Available from: http://www.specmaterials.com/siliconcarbidefiber.htm].
[22] Warrier SG, Rangaswamy P, Bourke MAM, Krishnamurthy S. Assessment of the fiber/matrix interface bond strength in SiC/Ti-6Al-4V composites. Mater Sci Eng A 1999;259(2):220–7.
[23] Ying Long, Athar Javed, Zhao-ke Chen, Xiang Xiong, Xiao P. Deposition rate, texture, and mechanical properties of SiC coatings produced by chemical vapor deposition at different temperatures. Int J Appl Ceram Technol 2013;10(1):11–9.
[24] Li Ju, Shan Zhiwei, Ma E. Elastic strain engineering for unprecedented materials properties. MRS Bull 2014;39:108–14.